



Where will the next flank eruption at Etna occur? An updated spatial probabilistic assessment

Laura Sandri¹, Alexander Garcia¹, Cristina Proietti², Stefano Branca², Gaetana Ganci², and Annalisa Cappello²

¹Istituto Nazionale di Geofisica e Vulcanologia, Sezione di Bologna, viale Carlo Berti-Pichat, 6/2, 40127 Bologna, Italy

²Istituto Nazionale di Geofisica e Vulcanologia, Osservatorio Etneo, piazza Roma, 1, Catania, Italy

Correspondence: Laura Sandri (laura.sandri@ingv.it)

Abstract. In this paper, we propose an update of the spatial probability map for flank eruptions from Etna (Italy), based on the distribution of the flank eruptive fissures that opened in the last 4000 years. The general procedure followed is to split the fissure dataset into training and testing subsets; then we build models on the training subset under different assumptions and test them on their likelihood of the testing subset. This allows selecting objectively the best models and assumptions. Furthermore, it allows testing whether (i) unavoidable incompleteness in the mapped fissures, and (ii) possible migration through time in the location of the flank activity, have an effect on the training models that can or cannot be neglected. We used different spatial models by exploiting different Kernel functions (Exponential, Cauchy, Uniform, and Gaussian), and calculated the degree of clustering of flank fissures in the training data. The results show that neither under-recording nor possible migration in time affect significantly the informativeness of the previous flank fissures in forecasting the location of the successive ones. Our study provides a canonical map of the spatial probability for future flank eruptions at Etna based on the location of flank fissures that opened in the last 4000 years. The map confirms a preferred location along a Northeast-to-South area, corresponding to the location of the most active rifts. It also shows that the Southern flank of the volcano, which is the most urbanized one, sits downhill of the largest cumulated-probability area for flank eruption. We also run sensitivity analyses to test the effect of (i) restricting the data to the most recent 400 years, and (ii) including the information on the unclamping stress induced on the mapped fissures by sources of deformation proposed in literature for recent eruptions of Etna. The results of the sensitivity analyses confirm the main features of the canonical map, and add information on the epistemic uncertainty attached to it.

1 Introduction

Etna is the most active volcano in Europe. It is a composite stratovolcano located along the Ionian coast of eastern Sicily and is characterized by a complex eruptive history that occurred over the last 500 ka (Branca et al., 2008, 2011a). Its four summit craters, Voragine, North-East Crater, Bocca Nuova and South-East Crater, display nearly continuous eruptive activity. At the summit craters, Strombolian activity and lava fountaining episodes are often associated with short-lasting lava flows (Alparone et al., 2003). Eruptive events also occur at intervals of years to tens of years from the flanks of the volcano. These flank eruptions are generally effusive and can be accompanied by explosive activity (Branca and Del Carlo, 2005).



25 The hazard posed by the summit explosive activity mostly affects tourism activities in terms of ballistics, pyroclastic density
currents, and lava flows, that can reach the summit pathways and tourism facilities located up to 2600 m a.s.l. (Proietti et al.,
2023). Furthermore, summit eruptions can occasionally significantly impact regional mobility as the tephra are dispersed into
the atmosphere under the action of winds. The tephra fallout can reach the airport in Catania (and sometimes Comiso and
Reggio Calabria) causing their partial or complete shutoff (Scollo et al., 2009). It can also blanket the local and national roads,
as happened throughout the 2021-2022 cluster of lava fountains (Calvari and Nunnari, 2022; Mereu et al., 2022).

30 Conversely, a relevant societal and economic threat on a larger spatial scale is posed by flank eruptions. In the last 400
years, lava flows from flank fissures (i.e. lateral eruptions) severely impacted inhabited areas on Etna flanks, causing property
loss and disruption of economic activities (Branca and Del Carlo, 2004). The 17th century saw the highest incidence of flank
eruptions that impacted the lower slopes of Etna and its urban fabric (Branca and Abate, 2019). Lateral lava flows caused
significant damage to the town of Bronte in 1651-53 and to Catania city in 1669 (Guidoboni et al., 2014), destroyed the suburb
35 of Linguaglossa in 1923 (Cerro and Catena), the town of Mascali in 1928, and threatened the town of Randazzo in 1981
(Chester et al., 2012; Coltelli et al., 2012; Branca et al., 2017). Most of these events had limited impact, except for the 1669
and 1928 eruptions. In particular, the 1669 eruption was the most destructive event on the Etna volcano in historical times. This
event conditioned the pattern of urbanization of the subsequent centuries and influenced the economic development across the
southeast flank of the volcanic edifice (Branca et al., 2013, 2015a, 2017). The 1928 eruption led to the destruction of the small
40 town of Mascali, and the cutting of road, railway, power and telecommunication lines. More recently, lava flows of the 2001
and 2002–2003 flank eruptions damaged the tourist facilities, which are located up to 2600 m elevation (Behncke and Neri,
2005). Occasionally, flank eruptions are accompanied by explosive activity, which, as in the case of summit eruptions, impacts
the mobility by tephra dispersal and fallout, such as in 1669 (Mulas et al., 2016), and in recent times, in 2001 (Andronico et al.,
2008) and 2002-2003 (Scollo et al., 2007).

45 In the last decades, rapid development has occurred on Etna's flanks, with the creation of a wide network of lifelines and
rapid growth of settlements (see Figure 1), often above lava flows from the historical period (Behncke and Neri, 2005). The
inhabited areas (see Figure 1) cover over 154km² and include the city of Catania (298,616 inhabitants, IST, February 2023)
and 41 more municipalities, with a total population of 1,029,107.

The geological history of Etna has been reconstructed by the new geological map of the volcano, which particularly details
50 the present volcanic center, *i.e.* the Mongibello volcano whose eruptive activity started about 15 ka (Branca et al., 2011a, b).
This dataset provides a detailed record of the spatial distribution of the volcanic products and of the eruptive fissures, as well
as of their stratigraphic relationships. In particular, the historical flank eruptions are chronologically well-constrained, thanks
to both the combination of stratigraphic and historiographical investigations, and to the dating of all the lava flows occurring
below roughly 2500 m of altitude. Above this altitude, the products of the post-17th century eruptions have almost covered
55 the summit portion of the volcano (Branca and Abate, 2019). Finally, after the mid-17th century the record of flank eruptions
is complete and accurate (Branca and Del Carlo, 2004). The flank eruptions of Mongibello show a gradual clustering of the
eruptive fissures. This evidences the development of some main weakness zones into the volcanic edifice, named North-East
(NE), South (S), and West (W) rifts (see Figure 1), in which the recurrent intrusion of feeder dykes occurred (Azzaro et al.,



2012). In this framework, the present state of the knowledge of the flank eruptions that occurred on Etna in the past 2500
60 years, performed by Branca and Abate (2019), has evidenced that these events most frequently involve the Southern sector,
thus highlighting that the S rift is the most active magma intrusion zone of Etna. In addition, temporal analysis of the elevation
of the eruptive fissures outlines that their opening at low elevation (< 1000 m a.s.l.) was common until the XVII century.
Following the 1669 eruption, the opening of fissures is mainly concentrated in the upper-middle slopes, between 1600 m and
2500 m a.s.l., and no flank eruptions have occurred below 1000 m of altitude (Branca and Abate, 2019).

65 Predicting the possible location of future flank eruptions is of paramount importance to minimize the potential impact of lava
flows on inhabited areas. On Etna, different approaches have been proposed to assess the probability of future vent opening by
analyzing the geology and distribution of historical eruptions and the processes driving magma transfer (see e.g. Guest and
Murray, 1979; Wadge et al., 1994; Behncke and Neri, 2005; Salvi et al., 2006; Cappello et al., 2013). Most of these approaches
have evaluated the spatial distribution of future volcanism through a probabilistic model based on the position of past eruptions.
70 As input data, they considered the eruptions of the last 500 (Salvi et al., 2006) or 400 years (Guest and Murray, 1979; Behncke
and Neri, 2005; Cappello et al., 2013), or even shorter recent periods (Wadge et al., 1994), owing to the lack of completeness
in the pre-1600 eruption record, and of the corresponding lava flow fields. The results of these analyses have confirmed the
NE, S, and W rifts (Figure 1) as the most prone areas.

In this paper, we perform a statistical analysis aimed at evaluating the spatial probability of future flank eruptions on Etna
75 based on the location of eruptive fissures having emplaced lateral lava flows during the last 4000 years. These data were
reconstructed by analysing the Etna New Geological Map (NGM, Branca et al., 2011b) and considering the eruptive products
having a lithostratigraphic position above the tephra layer related to the subplinian explosive eruption of picritic magma that
occurred 3930 ± 60 ka (FS tephra layer, Coltelli et al., 2005). We observe that flank eruptions in the last 4000 years are
comparable to current activity in terms of eruptive style, frequency, magnitude, and main features. Moreover, the last 4000
80 years of Mongibello's activity is the best known period in the entire eruptive history of the volcano (Branca et al., 2011a).
Thus, the data set that we consider for our analyses covers the last 4000 years.

As described in section 2, the first step of our work was to prepare the input data for the statistical analysis, namely the
position, direction and extent of the eruptive fissures of the last 4000 years. To this end, we first selected all the flank eruptions
in this time window from the last Etna's Geological Map (Branca et al., 2011a) and its following updates (Branca et al., 2015b;
85 Branca and Vigliotti, 2015; Branca and Abate, 2019). Then we prepared the input catalogue that includes both the main and
minor fissures of the selected eruptions. The main fissure of an eruption is defined as the one that fed the lava flow that had
the longest duration, covered the widest area, and the greatest distance from the vent (Proietti et al., 2011). All the remaining
fissures of an eruption are defined as minor ones.

In section 3 we describe the statistical model and the general strategy adopted, that consists in dividing the fissure input
90 catalogue to obtain independent training and testing sub-datasets. This allows setting up a reference model on the training
data based on specific hypotheses, and then testing it on new and independent data (the test data). In this way, we are able
to objectively judge the model performance. Further, if temporal coherence is kept among the training and testing data (i.e.:
training data are the older fissures, testing data are the younger ones), we can check whether there have been significant shifts



in the spatial pattern of flank activity, and/or systematic under-recording of past fissures in some areas. In other words, if
95 the test data are a plausible sample from the reference models built on the training data, we can reject with some degree of
confidence the hypothesis of a significant migration through time in the spatial distribution of flank fissures, and/or systematic
data incompleteness in some sectors of the volcano. With the training-testing strategy, we are also able to objectively identify
the best model among a set of competing ones, that we build to evaluate the sensitivity of our results to different assumptions
(section 3.4): the best model is the one that maximizes the likelihood of the test data. In particular we consider the sensitivity
100 to a different time window to select the input data, and to the orientation of flank fissures in a stress field. For the latter point, as
flank fissures can be oriented more or less favorably for unclamping normal stress for given deformation scenarios, we build up
alternative models that consider different plausible deformation sources at Etna volcano, taken from the literature (Bonaccorso
et al., 2006; Bonaccorso and Aloisi, 2021).

2 Data

105 2.1 Updating the fissure dataset

Starting from the Etna New Geological Map (NGM, Branca et al., 2011b) and the analysis of the catalogues and papers
describing Etna volcanic activity (Behncke and Neri, 2005; Branca and Del Carlo, 2005; Tanguy et al., 2012; Branca et al.,
2015b; Branca and Vigliotti, 2015; Branca and Abate, 2019), we considered a dataset of 193 flank eruptions occurred in the
last 4000 years in order to localise the fissures associated to these eruptive events. Concerning the historical eruptive fissures
110 covered by the eruptions that occurred from the XIX centuries, we integrated the dataset of the geological map of Branca et al.
(2011a) with previous 1:50.000 cartographies compiled by Sartorius Von Waltershausen (1848–61) and Romano et al. (1979)
and with the maps of the 1971-1991 eruptions (Azzaro and Neri, 1992). The analysis of the available datasets, performed in
the ESRI ArcGIS software (Version 10.6.0), allowed us to generate a shapefile for collecting the active portions of the eruptive
fissures. These fissures were traced on the base of their geological evidence, such as along the central axis of spatter ramparts
115 and scoria cones or at the main effusive vent of purely effusive eruptions. The dry portions of the fissures, i.e. which did not
give rise to eruptive activity, were not included in the dataset used in subsequent analyses. For each eruption, we considered all
the mapped flows, both the main and the minor ones, and we associated each of them with the corresponding fissure.

For some of the lava fields, it has not been possible to map the fissures, that had been later partially or totally buried by more
recent volcanic products. This was the case of minor lava fields or of other lava fields from purely effusive eruptions that were
120 covered in the proximal portion, i.e., near the vent.

We obtained a total of 190 fissures occurred in the last 4000 years that have been re-organized into 124 "systems of fissures".
Each system considers all the mapped fissures (both main and minor) that were active simultaneously in the same sector of
the volcano, i.e. that are related to the same eruptive event. In some cases (e.g., the 1978 eruptions in Valle del Bove, known
to have occurred distinctively over time at different periods, or the 1879 one whose fissures opened in two distinct sectors
125 of the volcano) the systems of fissures have been separated into different ones, as there was known separation in time and/or
space. Among the identified eruptions in the last 4000 years, only those that opened in the last 2500 years have been dated by



applying different techniques (Branca and Abate, 2019). For the older fissures, a common age of -2000CE was assigned, in order to label them as the oldest (older than 2500BP) in our input data set.

The set of fissures in the last 4000 years is shown in Figure 1a (colors represent the dated age).

130 2.2 Target domain

The target domain adopted for calculating the probability of vent opening for flank eruption is represented in Figure 1a (red dots): for simplicity, it is a rectangular regular grid of points (lower left and upper right centers are respectively (E=482590, N=4156090) and (E=514790, N=4191890) on the WGS84 33N UTM zone, with a grid spacing of 200 m), over which a mask covering the summit area (the polygon enclosing the summit caldera and craters) is applied. It consists of $N_C=28975$ grid cells.

135 In the supplementary material we provide a csv file containing the UTM coordinates and the elevation of each grid point.

3 Methods

We build the spatial probability of flank eruption, conditional to the occurrence of such an eruption at Mount Etna, with a spatial kernel method (Lutz and Gutmann, 1995). In order to account for the spatial extension and direction of fissures, we consider that the location and orientation of each fissure influence the spatial rate of flank opening as an elongated structure. In other words, in applying the classical kernel method, the rate of flank opening in a given point (x_P, y_P) of the target domain is affected by the N_f known past fissures by:

$$\lambda_{x_P, y_P} = \frac{\sum_{i=1}^{N_f} f(d_i; 0, h)}{N_f} \quad (1)$$

where d_i is the minimum distance between (x_P, y_P) and the i^{th} linear fissure element, $f(x; 0, h)$ is a probability density function of the kernel function adopted, with 0-mean and h smoothing parameter related to the dispersion around the mean (i.e., the standard deviation for the Gaussian case). The smoothing coefficient h is indicative of the degree of clustering between fissures (Martin et al., 2004), and must be determined by the available data, along with the best kernel function.

The spatial probability of future flank fissures opening in a given point (x_P, y_P) is computed by renormalizing λ_{x_P, y_P} over all the N_C grid cells on the considered domain:

$$Pr_{x_P, y_P} = \frac{\lambda_{x_P, y_P}}{\sum_{k=1}^{N_C} \lambda_{x_k, y_k}} \quad (2)$$

150 Given the large data set available for this study, we have the chance to divide the data into training and testing sets. In this way, we are able to set up different models on the training data (as input to equation 1), assuming different kernel functions and related parameter values. In such case, N_f corresponds to the number of fissures in the training set. The best combination of kernel function and smoothing parameter value is then selected by judging the capability of the different models to reproduce the testing data, which are new and independent data with respect to those used to set up the models.



155 Once the best combination of kernel function and smoothing parameter value is identified, the full data set (i.e., using both
training and testing fissures) is used for computing (through equation 2) a reference map of the spatial probability of future
flank fissure opening (that we call the *canonical* map).

3.1 Partition into training and testing data sets

There is no univocal method to partition the data into training and testing subsets. Here, to test both the effect of under-
recording of fissures as we go back in time, and of possible spatial migration in the flank activity with time, we partition the
160 input data into training and testing respecting temporal order, that is, training data are the older and testing data are the younger.
However, no sharp criterion on where to set the border between "older" and "younger" data exists. In Figure 1b we show the
Empirical Cumulative Distribution Function (ECDF) of the number of fissures in time. We highlight that, in the figure, the
large step at -2000CE (approximately 4000BP) is an artifact due to missing dates for systems of fissures older than 2500BP
165 (the grey area underlines this uncertainty), and thus they have been assigned a common age of -2000CE to build the ECDF.
In Figure 1b we also highlight (in red dashed lines) different dates corresponding to breaks in slope that can be subjectively
identified by visual inspection. Two of them can be related to changes in the recording capability of eruptions in the historical
record, or to changes in the eruption frequency: the partition at 1600 CE can be related to the fact that the catalogue of flank
eruptions is complete since the 17th century, whereas the 1971 partition can be associated with the increase in the lava output
170 and frequency of eruptions that began in 1971 (Branca and Del Carlo, 2004; Cappello et al., 2013), also related to the formation
of the South-East crater that formed as a pit crater in 1971 (Salvi et al., 2006; Del Negro et al., 2013; Rittman et al., 1971;
Branca et al., 2021). In order to set the border between training and testing data, we use the visual breaks in slope of the ECDF
shown in Figure 1b. Since there are three breaks in slope, we test 3 different partitions (see also table 1, first 3 rows); this allows
checking the stability of our results with different partition dates.

175 3.2 Identification of the best kernel function and degree of clustering

The first step in applying a spatial kernel method is to select a type of kernel function and the value for the smoothing coefficient.
In this study, we use the method proposed by Martin et al. (2004): by comparing the ECDF of the distance to the nearest
neighbor system of fissures to the cumulative distribution computed by using different kernel functions and suitable values of
the smoothing coefficient, we estimate the best pair of kernel function and smoothing coefficient for each training set in the
180 three different partitions of the data in the last 4000 years. In this work, we test 4 different possible kernel functions that all
decay with distance: Gaussian and Cauchy (as in Martin et al., 2004), and Exponential and Uniform (that we add in this study
to account for a rapidly-decaying smoothing and for a uniform-smoothing over a given distance, respectively). In practice, the
best pair selected is the one that best describes the ECDF of the distance of a system of fissures to its closest one. In this way,
we suppose that the distance among fissures of the same system does not influence the position of the next fissure that will
185 open. Instead, we assume that the future opening will be influenced by how close we are to another fissure system.



We repeat this operation for three partitions between training and testing datasets of fissures (first 3 rows in table 1) to test the stability of the results. Once the best pair for a given partition is selected, we build a reference probability model by applying equation 1 on the training data for that partition (table 1).

3.3 Model-performance evaluation

190 For each of the three reference models (one for each partition of the data in the last 4000 years), in order to judge their performance on the testing data, we repeat the following procedure.

First we compute the Log-Likelihood of observing the testing data under the reference model similarly to Marzocchi et al. (2016):

$$LL_{real} = \sum_{i=1}^{N_Y} \lambda_{x_i, y_i} + \sum_{i=1}^{N_N} (1 - \lambda_{x_i, y_i}) \quad (3)$$

195 where N_Y is the number of grid cells that host the trace of at least one test fissure, and N_N is the remaining number of grid cells (i.e. $N_N = N_C - N_Y$).

We then generate 100 synthetic catalogs of fissures based on the reference model, in which synthetic fissures are randomly placed on the target grid, with a higher chance where the reference model has larger λ . Each synthetic catalog consists of the same number of fissures as in the test dataset. Further, the length of each synthetic fissure is sampled without replacement from
200 the test catalog. This implies that the number of grid cells hosting a synthetic fissure is N_Y as for the real test data, and this is an important requirement for synthetic- and real-catalog Likelihoods to be comparable. In fact, for each j^{th} synthetic catalog, we compute the Log-Likelihood of observing the synthetic data under the reference model similarly to equation 3. By comparing the Log-Likelihood value of the real test data to the cumulative distribution of the 100 Log-Likelihood values of the synthetic catalogs, we can judge whether the real test data are a plausible sample of the reference model or if it is a very unlikely sample
205 (respectively if the p -value on the left tail $>$ or $\leq 5\%$).

3.4 Sensitivity analysis

So far, we have described the method to achieve a reference model, based on the data in the last 4000 years. In order to evaluate how much our results and tests change according to different hypothesis and assumptions, we repeat the model training and testing both considering (i) a shorter time window for the input data (i.e., since 1600CE), and (ii) the potential effects of other
210 phenomena such as the stress change on the mapped fissures induced by different plausible deformation source scenarios in recent Etna's eruptions, proposed in the literature (Bonaccorso et al., 2006; Bonaccorso and Aloisi, 2021).

3.4.1 Using only the data since 1600CE

As a first sensitivity analysis, we re-apply our strategy only considering the most recent part of the input data, that is the last 400 years, considered to be a complete catalogue of the flank eruptions at Etna. For this time window, we partition the data



215 into training and testing at 1900CE (table 1, bottom line). We remark that this time window neglects the older portion of the catalogue, that captures flank eruptions similar, in terms of eruptive style, frequency, magnitude, to the recent ones. However this time window is similar to that used in previous studies (Salvi et al., 2006; Guest and Murray, 1979; Behncke and Neri, 2005; Cappello et al., 2013).

3.4.2 Inclusion of stress changes due to different deformation sources

220 Theoretical studies have demonstrated that the trajectories of dikes underneath topography are affected by a balance among the topographic load, buoyancy forces, external stresses, and the free surface (e.g. Davis et al., 2021). Host rock stresses then influence magma pathways, and eruptive fissures tend to align themselves with the most energy-efficient orientation, which is roughly perpendicular to the least compressive principal stress axis (S₃, e.g. Anderson, 1951; Pollard, 1987; Dahm, 2000; Gudmundsson, 1995; Maccaferri et al., 2010; Roman and Jaupart, 2014; Rivalta et al., 2019). Eruptive fissures at the cone-shaped Etna volcano are oriented roughly following a radial pattern (see e.g., Figure 2); such pattern is directly correlated with the stress field in the volcanic cone, and this is the reason why we consider fissure orientation as a very informative parameter for the location of flank eruptions in this case.

When deformation processes take place underneath the volcano, it is possible to foresee changes in normal and shear stresses in fracture planes, the magnitude of which depends also on the orientation of the plane with respect to the deformation source. According to this observation, in this work we are interested in evaluating if changes in normal stresses on fracture planes, associated with different deformation scenarios, are informative to improve our spatial assessment of flank opening likelihood (by assuming that unclamping can favor fissure opening). In practice, we compute the normal component of the compressive stress change on the fissures in the catalog accounting separately for two possible sources of deformation (a volumetric source at depth feeding of the volcanic system, and a lateral slip of the Eastern flank of the volcano towards the Ionian sea) that have been proposed in recent literature (Bonaccorso et al., 2006; Bonaccorso and Aloisi, 2021) to explain the deformation patterns observed in GPS data. We also account for a linear combination of the stress change due to both sources if active simultaneously. We acknowledge that these two sources may not be active systematically and with the same intensity in a constant way: however, we argue that, when they are active, the assumption that the stress pattern (i.e., the relative stress difference over the fissures) does not change sign but is mostly enhanced or decreased depending on the deformation intensity and location, can be an acceptable at the first-order.

In order to compute the stress on a given fissure, we assume the fissure as the intersection with the Earth's surface of a vertical structure. We use Coulomb 3.3 (Toda et al., 2005; Lin and Stein, 2004) to compute the compressive stress change (normal and shear components) in vertically oriented fissures assuming the deformation caused by:

- a volumetric source of volume $7.9 \times 10^6 \text{ m}^3$ located at the point (UTM coordinates) X=499,634 m; Y=4,177,478 m; depth to the reference level (located at 1000 m a.s.l.)=3.9 km (we also performed tests varying the depth from 3.9 to 7.0 km below the reference level, without significant changes in the results)



- slip of the Eastern flank, with the coordinates of the top center of the plane as X=505,375 m; Y=4,172,644 m; depth (to reference level at 1000 m)=1.6 km; azimuth angle to north=8 degrees; length and width of the plane=20.3 and 25 km, respectively; dip angle=11.2 degrees; slip: -0.042 m (in strike direction) and -0.077m (in dip direction)

250 These sources are defined according to data from Table 2 in Bonaccorso et al. (2006).

We then assign a weight ω_i to each fissure depending on the sign and intensity of the normal component of the compressive stress, ranging from 0 (if the fissure is subject to clamping or neutral) to 1 (if it is the fissure with maximum unclamping stress). In Figures 2, 3 and 4 we show in tones of colours the normal stress change on the fissures in our dataset (negative/positive respectively for clamping/unclamping) according to the three sources of deformation considered in this study: volumetric, flank
255 slip and both of them. We then rebuild reference models for each of the partitions into training and testing reported in table 1, considering the weights due to the deformation source S as:

$$\lambda_{x_P, y_P}^S = \frac{\sum_{i=1}^{N_f} \omega_i f(d_i; 0, h)}{N_f \sum_{i=1}^{N_f} \omega_i} \quad (4)$$

For each partition, we then compute the Log-Likelihood of the model considering the deformation source S on the testing data, enabling the comparison with the un-weighted reference model by means of the Log-Likelihood difference: if the weighted
260 model that considers the deformation source S has a larger Likelihood on the testing data (positive Log-Likelihood difference) then it means that it outperforms the un-weighted model in explaining the testing data, and so it must be preferred, otherwise not.

We repeat this for each source of deformation (volumetric, flank slip, both), in each case identifying those fissures experiencing unclamping stress, i.e., those fissures located and oriented favourably for opening.

265 4 Results

4.1 Reference model on training data and test on independent data

In Figure 5a we show the comparison of the ECDF of the real training data (dots) with the theoretical cumulative distribution of the distance to the nearest system of fissures for the different types of kernel function explored (Gaussian, Cauchy, Exponential and Uniform) and different values of the smoothing coefficient h for the training set 4000BP-1600CE. The comparisons for
270 the other two partitions explored when considering the data from the last 4000 years, as well as all the other results for those two partitions, are provided in the Supplementary Material. We see that the Exponential model is always among the best ones in explaining the real ECDF, with best h values ranging from 500-1000 m for the partitions testing on recent data (1900CE or later) up to 1250 m when testing also on older data (see table 1). We see that the smoothing factor does not change dramatically when different boundaries between training and testing data are set.

275 In Figure 5b we show the ECDF of the Log-Likelihood of the synthetic testing datasets sampled from the reference model built with the Exponential kernel and smoothing factor $h = 1250$ m for the partition shown in Fig. 5a, with a red bar showing the value of the Log-Likelihood of the real testing data (i.e., the data between 1601CE and the present, see e.g., table 1). Based



on this analysis, we cannot reject the hypothesis of the reference models built on the training data by means of the Exponential kernel being able to explain the real testing data. This applies also to the other two partitions considered (see Supplementary
280 Material).

In Figure 6a we show the reference model built on the training data 4000BP-1600CE with the corresponding best combination in kernel function and smoothing parameter (i.e., for the case shown in Figure 5b and first row in table 1). For a visual inspection, we overlay the training and testing fissures.

4.2 Sensitivity analysis

285 In Figure 5c we show the same results of Figure 5a, when considering only the most recent portion of input data (last 400 year), with training set 1600CE-1900CE and testing set 1901CE-to-present. Also in this case the Exponential model is the best one in explaining the real ECDF, with best h value around 1000 m (see table 1, bottom line). In Figure 5d we show the ECDF of the Log-Likelihood of the synthetic testing datasets sampled from the reference models built with the Exponential kernel and smoothing factor $h = 1000$ m for the case of Figure 5c. Similarly to the case above, we cannot reject the hypothesis of the
290 reference models built on the training data by means of the Exponential kernel being able to explain the real testing data. The reference model built on the training data 1600CE-1900CE is shown in Figure 6b.

In Figure 6c-d we show the Log-Likelihood difference, compared to the reference models of the two cases shown in Figures 6a-b, of the models built when considering the orientation of fissures and the normal stress change due to different deformation sources, i.e. volumetric at approximately 3km depth (b.s.l.), flank slip towards East, and a combination of both (section 3.4.2).
295 We can see that the gain in model performance when weighting the training fissures according to their favoured orientation to unclamping stress is not univocal: the weighting according to the volumetric source of deformation is the one that maximizes the gain in likelihood in three out of four partitions (see also Supplementary Material for the training on 4000BP-1900CE and 4000BP-1970CE), except in the case of training on 1600CE-1900CE, where that model is rejected and the preferred is when using both volumetric and flank-slip source. In all of the examined cases, the flank-slip source by itself never gives rise to the
300 preferred model.

In the supplementary material we provide a csv file containing, for each grid point, the probability according to the canonical model and to all the sensitivity tests' models (8 models in total).

5 Discussion

5.1 A canonical spatial probability map for future flank fissures based on the last 4000 years of data

305 Based on our analysis of the position of flank fissures at Etna in the last 4000 years, a spatial map for flank fissure opening at Etna built with an Exponential kernel should be able to forecast better than chance the position of the future fissures. On one hand, the position of the past systems of fissures seems informative of the preferred positions of fissures that will open afterward. On the other hand, the results we have achieved by splitting the data into training and test subsets (Figure 5b-d)



show that (i) data incompleteness (unavoidable in such volcanic setting of high activity rate on a time period of thousands of
310 years) seems not to deteriorate the forecasting capability to an excessive degree, and that (ii) there is no significant evidence of
a systematic spatial migration in time during the past 4000 years. As a consequence, we propose a probabilistic model for the
opening of future flank fissures based on equation 1 and using the complete dataset of known fissures in the last 4000 years and
the largest smoothing parameter value for this case ($h=1250$ m, top row in table 1). This model, that we name "canonical", is
shown in Figure 7 (colors are represented using a logarithmic scale; see Supplementary for the linear scale). Overall, this map
315 clearly shows that the opening of fissures higher up towards the summit of the volcano (i.e., approximately above 1500 m a.s.l.)
has probabilities two-to-three orders of magnitude larger than positions located at low altitudes. This is expected due to the
higher density of fissures at higher elevations, and yet possibly underestimated by the overlapping of younger lava flows burying
older fissures. A clear North-to-SouthEast stretch in the probability pattern emerges, due to the density of fissures along the NE
and S rifts (e.g., Ruch et al., 2010). This North-to-SouthEast stretch also shows that, on the SSE flank, intermediate probability
320 values (10^{-5} to 10^{-4}) can be found at low altitudes, that is, down to approximately 300 m a.s.l., enclosing densely populated
areas immediately upstream from the city of Catania (for example the municipalities of Nicolosi, Mascalucia and Pedara, see
Figure 7). Moreover, on the SSE flank the probabilities are not negligible (10^{-6} to 10^{-5}) up to very low elevations, i.e. about
100 m a.s.l. In contrast, in the other directions the intermediate probabilities are found at altitudes greater than 1000 m a.s.l.
and enclosing inhabited areas only to a limited extent. With respect to the previously available maps in Cappello et al. (2012)
325 and Cappello et al. (2013), we see that our results confirm North-East to South-East pattern in the highest probability already
highlighted in those papers. Considering that the Mongibello flank eruptions showed a gradual clustering along the North-East,
South, and West rifts (Azzaro et al., 2012) we investigated if this clustering is confirmed by our probability analyses. In table 2
(first line) we show the cumulated probability of future flank opening in the different rift areas (these areas are shown in Figure
1 through dashed-dotted black lines). Since the spatial extent of the three rifts is very different ($NE \approx 18$ km²; $S \approx 119$ km²;
330 $W \approx 42$ km²), in table 2 we also show in brackets the probability normalized per unit area (per km²). The S rift has the highest
cumulated probability among the rifts. This result is coherent with the fact that the S rift has been the main zone of magma
intrusion for the last 2500 years (Branca and Abate, 2019). However, the S rift is by far the largest one, so a comparison on
the normalized probability per unit area is also useful: it shows that the NE rift is the one characterized by a spatial peak in
the probability, with normalized value about three to four times larger than for the W and S rifts, respectively. The W rift has
335 the lowest normalized probability value. For comparison, the cumulated probability of flank eruption outside the rifts is about
0.67 spread over a very large area, resulting in a probability per unit area of $7 \cdot 10^{-4}$ per km², that is an order of magnitude
lower than in the W rift, the lowest-probability one. We note that the S rift is the one much closer to, and partially covering,
areas characterized by intense urbanization. From a risk perspective, a more "diffuse" and less peaked spatial probability of a
future flank eruption on the S rift poses a hazard characterized by a large aleatory uncertainty (see e.g., Marzocchi and Jordan,
340 2014) on the Southern flank of the volcano. The S rift is also the one with non-negligible probability at the lowest elevations
and closest to urbanized areas: below 1000 m a.s.l. the cumulated probability of flank opening in the S rift is approximately
0.04, whereas below 500 m a.s.l., where most urbanization is found, it is around 0.03.



5.2 Sensitivity analysis: alternative maps

Considering only the flank fissures that opened in the most recent 400 years in equation 1 and the best kernel distribution for
345 this case (Exponential with $h=1000$ m, bottom row in table 1) yields the probabilistic model shown in Figure 8. Similarly to
the canonical model in Figure 7, this map confirms that high-altitude vent positions have larger probabilities. It shows higher
resolution details in probability changes (due to a smaller smoothing parameter value), but neglects the fact that distal fissures
have opened at Etna in the previous 3600 years, and indeed the probability pattern is more peaked at the higher altitudes (i.e.,
above 1500 m a.s.l.) and, at lower altitudes, has lower values than in the previous case. Similarly to the canonical map (Figure
350 7), the opening probability based on the last 400 y fissures shows a clear North-South stretch (Figure 8). However, compared
to the canonical map, it yields much lower values at elevations where inhabited areas are present, for example below 500 and
1000 m in the south and west slopes, respectively.

The addition of the information from the unclamping stress transferred from a volumetric source of deformation at depth
and/or an Eastward flank-slip movement does not univocally improve or deteriorate the forecast on the position of future
355 fissures: this analysis shows contrasting results when different partitions of training/testing data are assumed (Figure 6c-d).
When giving a higher weight to fissures favourably oriented to unclamping in response to a volumetric stress change (panels
a in Figures 9 and 10), the probabilistic pattern is roughly axisymmetrical. In all of the remaining cases, the North-to-South
stretch in the probability pattern appears as in the canonical map of Figure 7, especially when stress changes due to an Eastward
flank-slip are included (Figures 9b-c and 10b-c), due to the favoured orientation of many fissures in this condition.

360 For comparison with the canonical model of Figure 7, in table 2 we also provide the cumulated probability of future flank
opening in the different rift areas computed under the alternative models explored in the sensitivity analysis. The inclusion of
the effect of unclamping stress on fissures does not affect the main findings when the last 4000 years of data are used (rows 2-
3-4 in table 2). However, when we weight the fissures with the unclamping stress under a volumetric change in the deformation
pattern, the normalized probability in the W rift becomes the largest, whereas when the flank-slip mechanism is accounted for,
365 it becomes negligible compared to the other two rift areas.

Using only the last 4 centuries of data to build the probability maps does not change significantly these findings (rows 5 to
8 in table 2). The most evident effect is that, overall, the NE rift has larger probability values than those achieved using all the
last 4000 years of the fissure catalogue, and conversely the S rift probability decreases slightly.

In the Supplementary Material we provide the same maps (canonical model and alternative ones) using a linear scale for the
370 color ramp.

After completing the data analysis and model setup for this paper, at the beginning of June 2022, there were 3 active vents
producing lava flows on Etna (<https://www.ct.ingv.it/Dati/informative/vulcanico/ComunicatoETNA20220612201349.pdf>). Their
location is shown in Figures 7, 8, 9 and 10 (points labelled A, B and C). Since these vents had not been used in building the
probability maps, their position is tested to check whether they have opened in high-probability areas. In table 2 we show the
375 overall percentiles of these 3 vents in the distributions computed on the basis of different data periods (data since 4000BP or
1600CE) and deformation models. In all the cases we see that the vents active in June 2022 opened in areas with probabilities



well above the 95th percentile, and in most of the combinations of data periods and deformation models the points A and B are above the 99th percentile. We consider this a small evidence in favour of our maps being an informative and quantitative tool to forecast the position of future vents.

380 6 Conclusions

In this work, we have reconstructed the most complete and up-to-date catalogue of flank fissures at Etna that opened in the last 4000 years, based on the most recent and complete update of the geological map of Etna, which represents significant progress in the geological studies of this volcano over the last 30 years (Branca et al., 2011b).

We have used this catalogue to build a spatial probability model for fissure opening in future flank eruptions at Etna. The
385 proposed model extends and improves the previous ones available in the literature, as the temporal range that our input data cover (4000 years) is larger with respect to previous works (up to 500 years, Guest and Murray, 1979; Behncke and Neri, 2005; Wadge et al., 1994; Salvi et al., 2006; Cappello et al., 2013), and it is based on a more complete and updated geological map.

Since the reconstructed catalogue is composed by over 120 systems of fissures, we were able to split the data into training
390 and testing subsets. This allowed us to perform an objective evaluation of the model performance on independent data with respect to those used in the model setup. It also allowed excluding that the unavoidable (over a time interval of 4000 years) data incompleteness significantly deteriorate the forecasting capability of the location of flank fissures based on the position of previous ones. Finally, it excluded a systematic and significant spatial migration in time during the past 4000 years.

The proposed canonical model shows that high altitude flank fissures are more likely by two-to-three orders of magnitude
395 respect to the lower altitude ones. It also confirms a North-East to South-East pattern of higher probability, which involves the highest urbanized flank immediately upstream from the city of Catania, as already found by Cappello et al. (2012) and Cappello et al. (2013).

In order to check the effects of the hypothesis and assumptions of our model, we build alternative models based on (i) a shorter time window of data (only the last 400 years, a period that is considered complete in terms of flank fissure recording),
400 and (ii) a weighting of the past fissures according to the unclamping stress exerted by changes in the normal stress due to different deformation patterns at depth. We considered two deformation sources proposed in the recent literature (Bonaccorso et al., 2006; Bonaccorso and Aloisi, 2021), i.e. a volumetric source at depth and an Eastward flank-slip of the Eastern flank of Etna, and a combination of the two. The canonical map based on the last 4000 years shows non-negligible probabilities at elevations lower than that based on the last 400 years. This result is in agreement with the opening of fissures at low altitudes
405 (below 1000 m a.s.l.) observed before the 1669 CE eruption, and subsequently with their greater concentration in the mid- to upper slopes (Branca and Abate, 2019). Both the maps based on the last 4000 and 400 years show that the three rifts (NE, S and W, Azzaro et al., 2012) are the areas with highest probability per unit area of flank fissure opening. The low elevations to which the probability of opening on the S rift extends, especially when considering the canonical map, and the intense urbanization within this area, imply a high risk there.



410 We argue that averaging the canonical map and the alternative ones into a single, weighted map, may not be the best solution for two reasons. First, in a potential unrest characterized by a specific deformation pattern, having separate vent-opening maps based on alternative deformation source models allows for giving more credit to the map based on the deformation pattern that is similar to the ongoing one. Secondly, in case the vent-opening maps are used for hazard assessment (for example, coupling them to simulations of lava flows or tephra dispersal from different vents, e.g. Del Negro et al., 2013; Selva et al., 2010; 415 Martinez Montesinos et al., 2022), a portfolio of vent-opening maps allows a disaggregation of the contribution to the total hazard. In this view, the canonical map and the alternative ones encompass and quantify the epistemic uncertainty.

Data availability. In the supplementary we provide, in csv format, the resulting probability maps under the different models proposed in the paper.

Author contributions. LS, AG, GG, AC conceived the study. CP and SB extracted the data from the New Geological Map. AG computed the stress on the vertical faults. LS and AG conceived the method, analysed the data and the results. LS wrote the manuscript, with input from all 420 the authors. AG prepared with QGIS the maps shown in figures, with input data from the authors. All the authors reviewed the manuscript.

Competing interests. The authors declare no competing interests.

Acknowledgements. The authors wish to thank Mauro Coltelli for thorough discussions about the data and results, that helped improving the study.

425 This work was supported by the INGV project Pianeta Dinamico (CUP D53J19000170001) funded by MIUR (“Fondo finalizzato al rilancio degli investimenti delle amministrazioni centrali dello Stato e allo sviluppo del Paese,” legge 145/2018), Tema 8 – PANACEA 2021-2023.



References

- IstatData - La banca dati dell'Istituto Nazionale di Statistica, <http://dati.istat.it/Index.aspx?QueryId=18976#>, accessed: 2023-05-09.
- 430 Alparone, S., Andronico, D., Lodato, L., and Sgroi, T.: Relationship between tremor and volcanic activity during the Southeast Crater eruption on Mount Etna in early 2000, *J. Geophys. Res. Solid Earth*, 108 (B5), <https://doi.org/10.1029/2002JB001866>, 2003.
- Anderson, E. M.: *The Dynamics of Faulting and Dyke Formation with Applications to Britain*, Oliver and Boyd, ed. 2, 1951.
- Andronico, D., Scollo, S., Caruso, S., and Cristaldi, A.: The 2002–03 Etna explosive activity: tephra dispersal and features of the deposits, *J. Geophys. Res. Solid Earth*, 113 (B4), <https://doi.org/10.1029/2007JB005126>, 2008.
- 435 Azzaro, R. and Neri, M.: L'attività eruttiva dell'Etna nel corso del ventennio 1971–1991. Primi passi verso la costituzione di un data-base relazionale, CNR IIV Open File Report, 3, 46, 1992.
- Azzaro, R., Branca, S., Winner, K., and Coltelli, M.: The volcano-tectonic map of Etna volcano, 1:100.000 scale: an integrated approach based on a morphotectonic analysis from high-resolution DEM constrained by geologic, active faulting and seismotectonic data, *Ital.J.Geosci. (Boll.Soc.Geol.It.)*, 131, 1, 153–170, <https://doi.org/10.3301/IJG.2011.29>, 2012.
- 440 Behncke, B. and Neri, M.: Lava flow hazard at Mount Etna (Italy): new data from a GIS-based study, *SPECIAL PAPERS - GEOLOGICAL SOCIETY OF AMERICA*, 396, 189, 2005.
- Bonaccorso, A. and Aloisi, M.: Tracking Magma Storage: New Perspectives From 40 Years (1980–2020) of Ground Deformation Source Modeling on Etna Volcano, *Frontiers in Earth Science*, 9, <https://doi.org/10.3389/feart.2021.638742>, 2021.
- Bonaccorso, A., Bonforte, A., Guglielmino, F., M, P., and Puglisi, G.: Composite ground deformation pattern forerunning the 2004–2005 Mount Etna eruption, *J. Geophys. Res.*, 111, B12207, 2083–2094, <https://doi.org/10.1029/2005JB004206>, 2006.
- 445 Branca, S. and Abate, T.: Current knowledge of Etna's flank eruptions (Italy) occurring over the past 2500 years. From the iconographies of the XVII century to modern geological cartography, *J. Volcanol. Geotherm. Res.*, 385, 159–178, 2019.
- Branca, S. and Del Carlo, P.: Eruptions of Mt. Etna during the past 3,200 years: A revised compilation integrating the historical and stratigraphic records, in: *Mt. Etna, volcano laboratory*, edited by Bonaccorso, A., Calvari, S., Coltelli, M., Del Negro, C., and Falsaperla, S., pp. 1–27, *American Geophysical Union Geophysical Monograph* 143, 2004.
- 450 Branca, S. and Del Carlo, P.: Types of eruptions of Etna volcano AD 1670-2003: implications for short-term eruptive behavior, *Bull. Volcanol.*, 67, 732–742, 2005.
- Branca, S. and Vigliotti, L.: Finding of an historical document describing an eruption in the NW flank of Etna in July 1643 AD: timing, location and volcanic products, *Bull. Volcanol.*, 77 (11), 1–6, 2015.
- 455 Branca, S., Coltelli, M., De Beni, E., and Wijbrans, J.: Geological evolution of Mount Etna volcano (Italy) from earliest products until the first central volcanism (between 500 and 100 ka ago) inferred from geochronological and stratigraphic data, *Int. J. Earth Sci. (Geol. Rundsch.)*, 97, 135–152, 2008.
- Branca, S., Coltelli, M., and Groppelli, G.: Geological evolution of a complex basaltic stratovolcano: Mount Etna, *Ital. J. Geosci.*, 130 (3), 306–317, 2011a.
- 460 Branca, S., Coltelli, M., Groppelli, G., and Lentini, F.: Geological map of Etna volcano, 1:50,000 scale, *Ital. J. Geosci.*, 130 (3), 265–291, <https://doi.org/10.3301/IJG.2011.15>, 2011b.
- Branca, S., De Beni, E., and Proietti, C.: The large and destructive 1669 AD eruption at Etna volcano: reconstruction of the lava flow field evolution and effusion rate trend, *Bull. Volcanol.*, 75 (2), 1–16, <https://doi.org/10.1007/s00445-013-0694-5>, 2013.



- Branca, S., Azzaro, R., De Beni, E., Chester, D., and Duncan, A.: Impacts of the 1669 eruption and the 1693 earthquakes on the Etna Region (Eastern Sicily, Italy): An example of recovery and response of a small area to extreme events, *J. Volcanol. Geotherm. Res.*, 303, 25–40, 2015a.
- Branca, S., Condomines, M., and Tanguy, J. C.: Flank eruptions of Mt Etna during the Greek–Roman and Early Medieval periods: New data from 226Ra–230Th dating and archaeomagnetism, *J. Volcanol. Geotherm. Res.*, 304, 265–271, 2015b.
- Branca, S., De Beni, E., Chester, D. K., Duncan, A. M., and Lotteri, A.: The 1928 eruption of Mount Etna (Italy): Reconstructing lava flow evolution and the destruction and recovery of the town of Mascali, *J. Volcanol. Geotherm. Res.*, 335, 54–70, 2017.
- Branca, S., Musumeci, D., and Ingaliso, L.: The significance of the 1971 flank eruption of Etna from volcanological and historic viewpoints, *Ann. Geophysics*, 64, VO543, <https://doi.org/10.4401/ag-8669>, 2021.
- Calvari, S. and Nunnari, G.: Comparison between Automated and Manual Detection of Lava Fountains from Fixed Monitoring Thermal Cameras at Etna Volcano, Italy, *Remote Sens.*, 14, 2392, <https://doi.org/10.3390/rs14102392>, 2022.
- Cappello, A., Neri, M., Acocella, V., Gallo, G., Vicari, A., and Del Negro, C.: Spatial vent opening probability map of Mt Etna volcano (Sicily, Italy), *Bull. Volcanol.*, 74, 2083–2094, <https://doi.org/10.1007/s00445-012-0647-4>, 2012.
- Cappello, A., Bilotta, G., Neri, M., and Del Negro, C.: Probabilistic modeling of future volcanic eruptions at Mount Etna, *J. Geophys. Res.: Solid Earth*, 118, 1–11, <https://doi.org/10.1002/jgrb.50190>, 2013.
- Chester, D. K., Duncan, A. M., and Sangster, H.: Human responses to eruptions of Etna (Sicily) during the late-Pre-Industrial Era and their implications for present-day disaster planning, *J. Volcanol. Geotherm. Res.*, 225–226, 65–80, <https://doi.org/10.1016/j.jvolgeores.2012.02.017>, 2012.
- Coltelli, M., Del Carlo, P., Pompilio, M., and Vezzoli, L.: Explosive eruption of a picrite: the 3930 BP subplinian eruption of Etna volcano (Italy), *Geophys. Res. Lett.*, 32, L23307, <https://doi.org/10.1019/2005GL024271R>, 2005.
- Coltelli, M., Marsella, M., Proietti, C., and Scifoni, S.: The case of the 1981 eruption of Mount Etna: An example of very fast moving lava flows, *Geochem. Geophys. Geosyst.*, 13, Q01004, <https://doi.org/10.1029/2011GC003876>, 2012.
- Dahm, T.: Numerical simulations of the propagation path and the arrest of fluid-filled fractures in the Earth, *Geophysical Journal International*, 141, 623–638, <https://doi.org/10.1046/j.1365-246x.2000.00102.x>, 2000.
- Davis, T., Bagnardi, M., Lundgren, P., and Rivalta, E.: Extreme Curvature of Shallow Magma Pathways Controlled by Competing Stresses: Insights From the 2018 Sierra Negra Eruption, *Geophysical Research Letters*, 48, e2021GL093038, <https://doi.org/10.1029/2021GL093038>, e2021GL093038 2021GL093038, 2021.
- Del Negro, C., Cappello, A., Neri, M., Bilotta, G., Herault, A., and Ganci, G.: Lava flow hazards at Mount Etna: constraints imposed by eruptive history and numerical simulations, *Sci Rep*, 3, <https://doi.org/10.1038/srep03493>, 2013.
- Gudmundsson, A.: Infrastructure and mechanics of volcanic systems in Iceland, *Journal of Volcanology and Geothermal Research*, 64, 1–22, [https://doi.org/10.1016/0377-0273\(95\)92782-Q](https://doi.org/10.1016/0377-0273(95)92782-Q), 1995.
- Guest, J. E. and Murray, J. B.: An analysis of hazard from Mount Etna volcano, *Journal of the Geological Society*, 136, 347–354, <https://doi.org/10.1144/gsjgs.136.3.0347>, 1979.
- Guidoboni, E., Ciuccarelli, C., Mariotti, D., Comastri, A., and Bianchi, M. G.: L’Etna nella storia. Catalogo delle eruzioni dall’antichità alla fine del XVII sec., Bononia University Press, Bologna, 2014.
- Lin, J. and Stein, R. S.: Stress triggering in thrust and subduction earthquakes and stress interaction between the southern San Andreas and nearby thrust and strike-slip faults, *Journal of Geophysical Research: Solid Earth*, 109, <https://doi.org/10.1029/2003JB002607>, 2004.



- Lutz, T. M. and Gutmann, J. T.: An improved method for determining and characterizing alignments of point like features and its implications for the Pinacate volcanic field, Sonora, Mexico, *J. Geophys. Res.*, 100, 17 659–17 670, 1995.
- Maccaferri, F., Bonafede, M., and Rivalta, E.: A numerical model of dyke propagation in layered elastic media, *Geophysical Journal International*, 180, 1107–1123, <https://doi.org/10.1111/j.1365-246X.2009.04495.x>, 2010.
- 505 Martin, A., Umeda, K., Connor, C., Weller, J., Zhao, D., and Takahashi, M.: Modeling long-term volcanic hazards through Bayesian inference: An example from the Tohoku volcanic arc, Japan, *J. Geophys. Res. Solid Earth*, 109, B10, <https://doi.org/10.1029/2004JB003201>, 2004.
- Martinez Montesinos, B., Luzón, M., Sandri, L., Rudy, O., Cheptsov, A., Macedonio, G., Folch, A., Barsotti, S., Selva, J., and Costa, A.: On the feasibility and usefulness of high performance computing in probabilistic volcanic hazard assessment: An application to tephra hazard from Campi Flegrei, *Front. Earth Sci.*, 10:941789, <https://doi.org/10.3389/feart.2022.941789>, 2022.
- 510 Marzocchi, W. and Jordan, T.: Testing for ontological errors in probabilistic forecasting models of natural systems, *Proc Natl Acad Sci USA*, 111, 11 973–11 978, <https://doi.org/10.1073/pnas.1410183111>, 2014.
- Marzocchi, W., Sandri, L., Heuret, A., and Funicello, F.: Where giant earthquakes may come, *J. Geophys. Res. Solid Earth*, 121, <https://doi.org/10.1002/2016JB013054>, 2016.
- 515 Mereu, L., Stocchi, K., Garcia, A., Prestifilippo, M., Sandri, L., Bonadonna, C., and Scollo, S.: Quantification of tephra mass deposited on road network during lava activity in 2021–22 at Mt. Etna, in: *Abstract Volume 5 Conferenza A. RITTMANN*, edited by Cocina, O., Tranne, C., Vona, A., and Viccaro, M., pp. 1–340, *Misc. INGV*, 70, <https://doi.org/10.13127/misc/70>, 2022.
- Mulas, M., Cioni, R., Andronico, D., and Mundula, F.: The explosive activity of the 1669 Monti Rossi eruption at Mt. Etna (Italy), *J Volcanol Geotherm Res*, 328, 115–133, 2016.
- 520 Pollard, F.: Elementary fracture mechanics applied to the structural interpretation of dikes, *Geol. Assoc. Can. Spec.*, 34, 112–128, 1087.
- Proietti, C., De Beni, E., Coltelli, M., and Branca, S.: RThe flank eruption history of Etna (1610–2006) as a constraint on lava flow hazard, *Ann. Geophysics*, 54, <https://doi.org/10.4401/ag-5333>, 2011.
- Proietti, C., De Beni, E., Cantarero, M., Ricci, T., and Ganci, G.: Rapid provision of maps and volcanological parameters: quantification of the 2021 Etna volcano lava flows through the integration of multiple remote sensing techniques, *Bull. Volcanol.*, 85, <https://doi.org/10.1007/s00445-023-01673-w>, 2023.
- 525 Rittman, A., Romano, R., and Sturiale, C.: L'eruzione etnea dell'aprile–giugno 1971, *Atti Accad. Gioenia Sci. Nat. (Catania)*, pp. 1–29, 1971.
- Rivalta, E., Corbi, F., Passarelli, L., Acocella, V., Davis, T., and Di Vito, M. A.: Stress inversions to forecast magma pathways and eruptive vent location, *Science Advances*, 5, eaau9784, <https://doi.org/10.1126/sciadv.aau9784>, 2019.
- 530 Roman, A. and Jaupart, C.: The impact of a volcanic edifice on intrusive and eruptive activity, *Earth and Planetary Science Letters*, 408, 1–8, <https://doi.org/10.1016/j.epsl.2014.09.016>, 2014.
- Romano, R., Lentini, F., and Sturiale, C.: Carta geologica del Monte Etna: Geological map of Mt. Etna, in: *Progetto finalizzato Geodinamica. Istituto internazionale di vulcanologia*, edited by Cartografica, L. A., Consiglio nazionale delle ricerche (Italy), Catania, 1979.
- Ruch, J., Acocella, V., Storti, F., Neri, M., Pepe, S., Solaro, G., and Sansosti, E.: Detachment depth of an unstable volcano revealed by rollover deformation: an integrated approach at Mt. Etna, *Geophys Res Lett*, 37, L16 304, <https://doi.org/10.1029/2010GL044131>, 2010.
- 535 Salvi, F., R, S., and C, P.: Statistical analysis of the historical activity of Mount Etna, aimed at the evaluation of volcanic hazard, *Journal of Volcanology and Geothermal Research*, 154, 159–168, <https://doi.org/10.1016/j.jvolgeores.2006.01.002>, 2006.
- Sartorius Von Waltershausen, W.: *Atlas des Aetna*, S. Schmidt (v. 1), Berlin, Geografisches Institut (voll. 2–8); Weimar (9), 1848–61.



- Scollo, S., Del Carlo, P., and Coltelli, M.: Tephra fallout of 2001 Etna flank eruption: analysis of the deposit and plume dispersion, *J. Volcanol. Geotherm. Res.*, 160, <https://doi.org/10.1016/j.jvolgeores.2006.09.007>, 2007.
- 540 Scollo, S., Prestifilippo, M., Spata, G., D'Agostino, M., and Coltelli, M.: Monitoring and forecasting Etna volcanic plumes, *Nat. Hazards Earth Syst. Sci.*, 9, 1573–1585, <https://doi.org/10.5194/nhess-9-1573-2009>, 2009.
- Selva, J., Costa, A., Marzocchi, W., and Sandri, L.: BET_VH: exploring the influence of natural uncertainties on long-term hazard from tephra fallout at Campi Flegrei (Italy), *Bull. Volcanol.*, 72, 717–733, <https://doi.org/10.1007/s00445-010-0358-7>, 2010.
- 545 Tanguy, J. C., Condomines, M., Branca, S., La Delfa, S., and Coltelli, M.: New archeomagnetic and ²²⁶Ra-²³⁰Th dating of recent lavas for the Geological map of Etna volcano, *Italian Journal of Geosciences*, 131(2), 241–257, 2012.
- Toda, S., Stein, R. S., Richards-Dinger, K., and Bozkurt, S. B.: Forecasting the evolution of seismicity in southern California: Animations built on earthquake stress transfer, *Journal of Geophysical Research: Solid Earth*, 110, <https://doi.org/10.1029/2004JB003415>, 2005.
- Wadge, G., Young, P. A., and Mckendrick, I. J.: Mapping lava flow hazards using computer simulation, *Journal of Geophysical Research*, 99, 550 <https://doi.org/10.1029/93JB01561>, 1994.

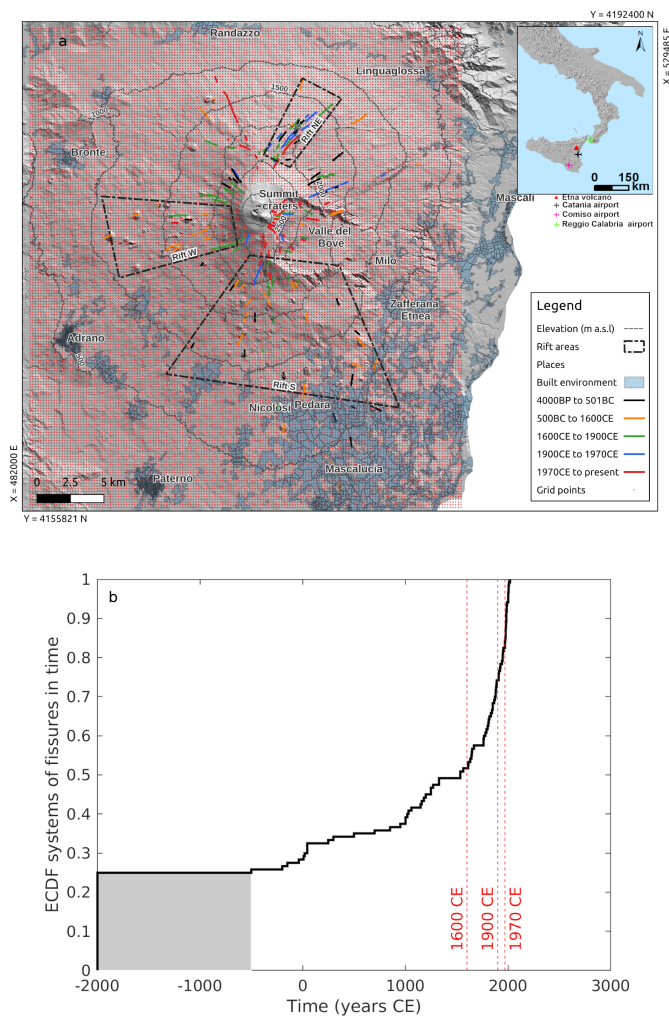


Figure 1. (a): grid (red dots) and fissures (different colors depending on their age, see legend) used in this study. The location and extent of the built environment is shown as shaded pale blue areas. The three main rifts (NorthEast -NE-, South -S-, and West -W-) (according to Azzaro et al., 2012) are shown in black dashed-dotted lines. Altitude contour lines are shown in thin dashed black lines. The inset shows the location of Etna Volcano in Southern Italy, and the main airports that can be affected by its activity. (b): Empirical Cumulative Distribution Function (ECDF) of the systems of fissures in time (black solid line). The red dotted lines indicate the different breaks in time used to partition the data into training and testing. The grey-shaded area underlines the uncertainty on the age of events older than 2500BP.



Calculated Normal stress change in fissures assuming a volumetric source (source parameters from Bonaccorso et al 2006)

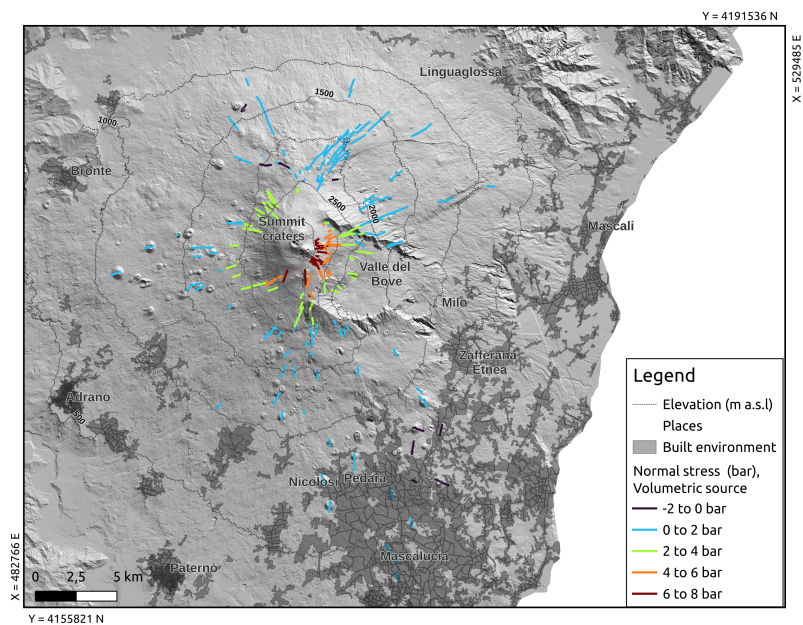


Figure 2. Normal stress change on fissures in the catalog, when a volumetric source of deformation at depth is placed, as in Bonaccorso et al. (2006) (positive values indicate unclamping; Poisson ratio 0.25; Young's modulus 8.0×10^5 bar). The location and extent of the built environment is shown in dark gray shaded areas.

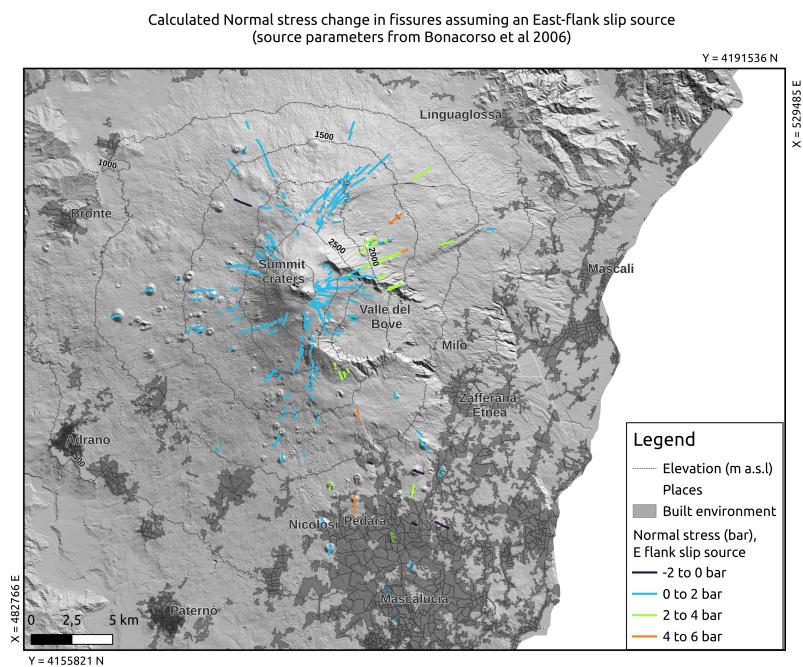


Figure 3. Normal stress change on fissures in the catalog, when an Eastward flank-slip source of deformation at depth is placed, as in Bonaccorso et al. (2006) (positive values indicate unclamping; Poisson ratio 0.25; Young's modulus 8.0×10^5 bar). The location and extent of the built environment is shown in dark gray shaded areas.

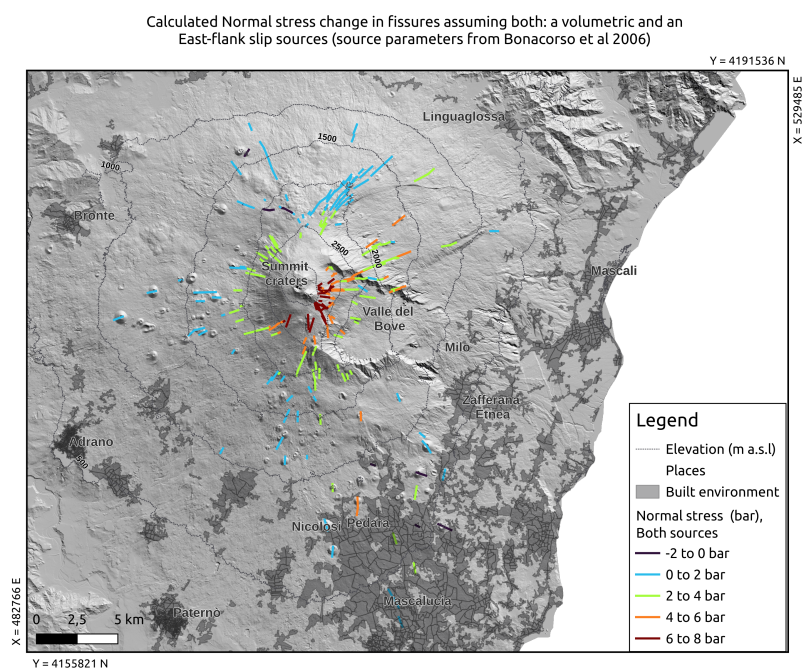


Figure 4. Normal stress on fissures in the catalog, when both a volumetric and an Eastward flank-slip sources of deformation at depth are placed, as in Bonaccorso et al. (2006) (positive values indicate unclamping; Poisson ratio 0.25; Young's modulus 8.0×10^5 bar). The location and extent of the built environment is shown in dark gray shaded areas.

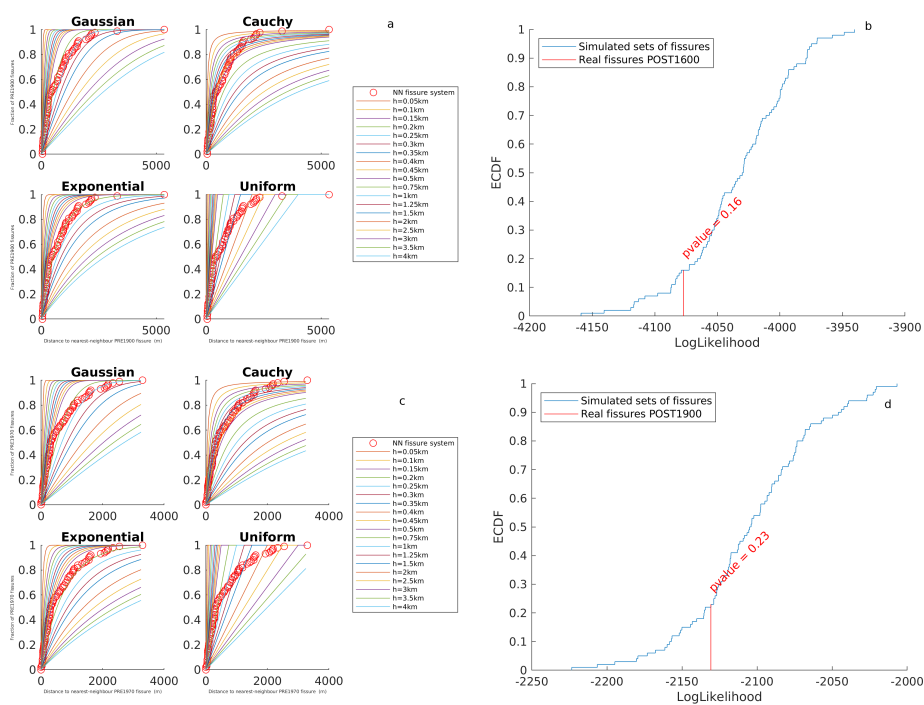


Figure 5. Panels a and c: Empirical Cumulative Density Functions (ECDF) of the distance to the nearest system of fissures (red dots) for the training period 4000BP-1600CE (a) and 1600CE-1900CE (c). The curves represent the theoretical cumulative for different kernel functions (Gaussian, Cauchy, Exponential and Uniform) and smoothing parameter h , as in legends on the right for each case. Panels b and d: ECDF of the Log-Likelihood of synthetic catalogs of synthetic fissures (black line) under the reference model for the training period (b) 4000BP-1600CE (Exponential kernel, $h=1250$ m) and (d) 1600CE-1900CE (Exponential kernel, $h=1000$ m). In red we point the value of the Log-Likelihood achieved by the reference model on the real testing data, providing the p -value in percent.

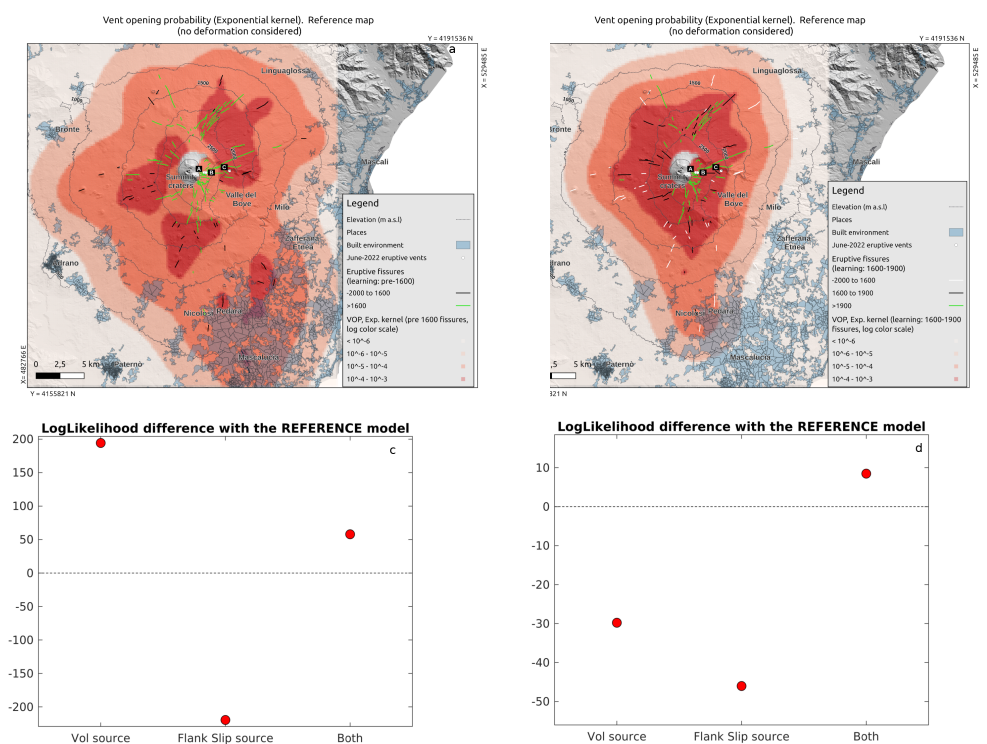


Figure 6. Panels a-b: Spatial probability (in Log-scale) distribution of flank opening under the reference model for the training period 4000BP-1600CE (a) and 1600CE-1900CE (b). In black and green the training and testing (i.e., respectively post 1600CE and post 1900CE for a and b) fissures. In panel b, in white solid lines we show the fissures older than 1600 CE, which are not used in the case of panel b. Panels c-d: Log-Likelihood difference between the models weighted with the three deformation sources explored (Volumetric, Flank Slip and Both) and the reference model of panels a and b, respectively. Positive differences (values above the dashed line) indicate a best performance on the testing data with respect of the reference model.

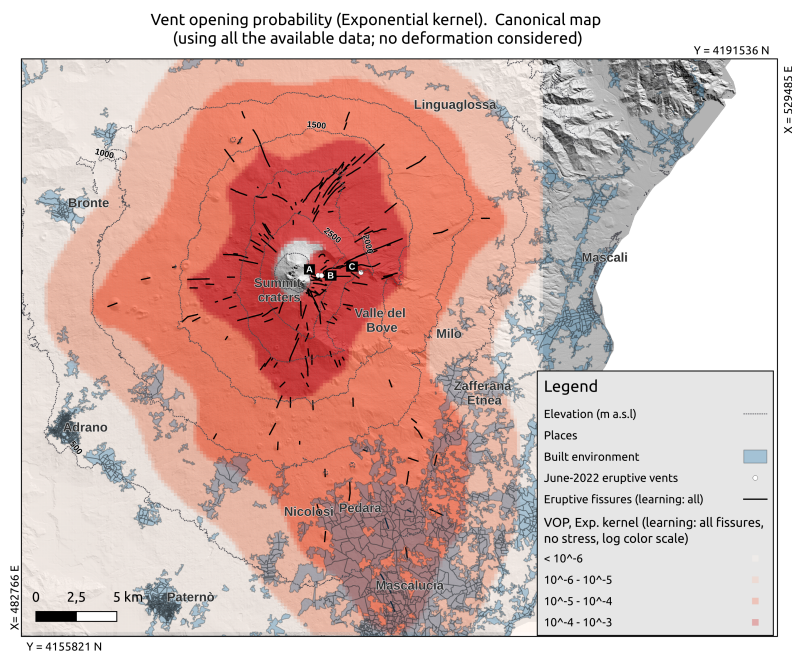


Figure 7. Map of the probability (Log scale) of flank fissure opening at Etna, based on the data 4000BP-present (black solid lines), in what we call canonical model. The location of the vents active in June 2022 is indicated by white points and labelled as A, B and C. The location and extent of the built environment is shown as shaded pale blue areas, and altitude contour lines are shown in dashed black lines.

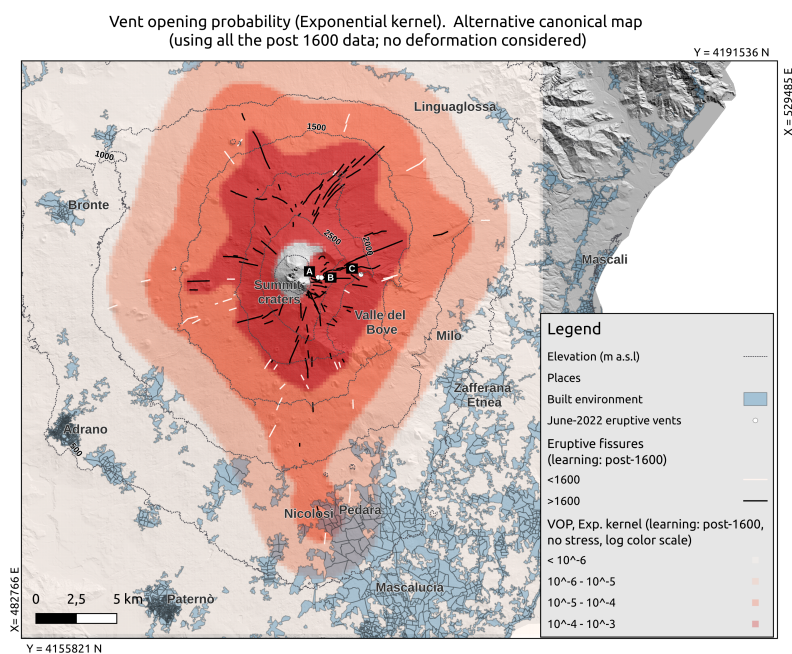


Figure 8. Result of the sensitivity analysis: map of the probability (Log scale) of flank fissure opening at Etna, based on a shorter time window for input data (1600CE-present, black solid lines). The location of the vents active in June 2022 is indicated by white points and labelled as A, B and C. The location and extent of the built environment is shown as shaded pale blue areas, and altitude contour lines are shown in dashed black lines. In white solid lines we show the oldest fissures (4000BP-1599 CE) not used in these maps.

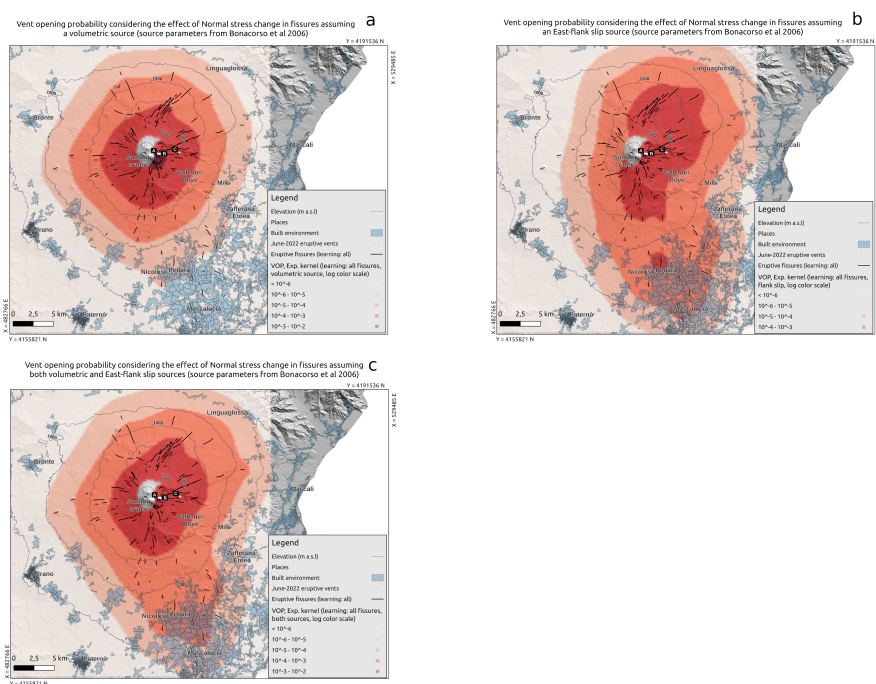


Figure 9. Sensitivity analysis: maps of the probability (Log scale) of flank fissure opening at Etna, based on the data 4000BP-present (black solid lines), considering the unclamping stress in the input fissures. The different panels a, b and c correspond to, respectively, information from the volumetric, flank-slip and both sources. In each panel, the location of the vents active in June 2022 is indicated by white points and labelled as A, B and C. The location and extent of the built environment is shown as shaded pale blue areas.

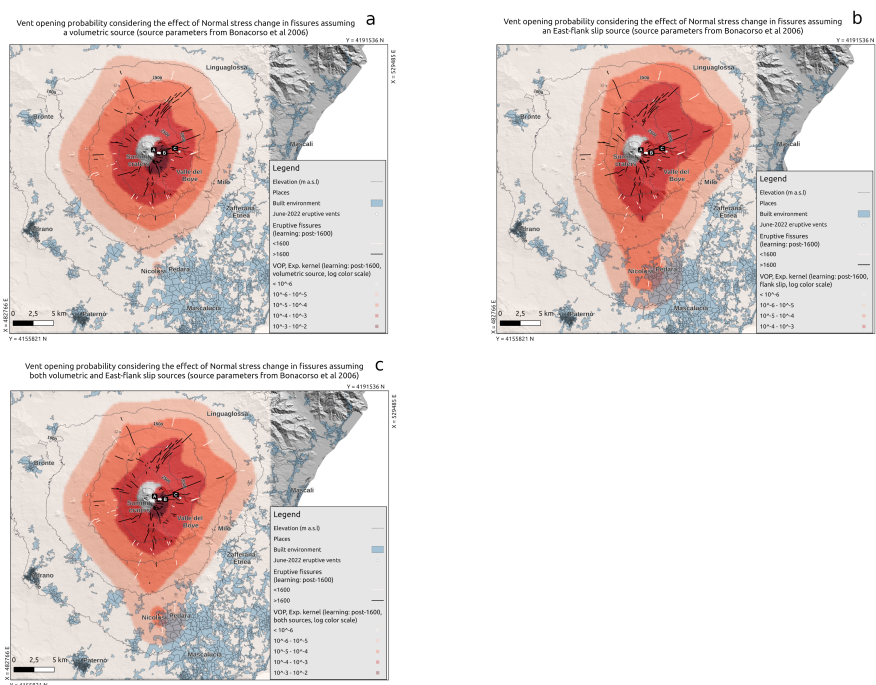


Figure 10. Sensitivity analysis: maps of the probability (Log scale) of flank fissure opening at Etna, based on the data 1600BP-present (black solid lines), considering the unclamping stress in the input fissures. The different panels a, b and c correspond to, respectively, information from the volumetric, flank-slip and both sources. In each panel, the location of the vents active in June 2022 is indicated by white points and labelled as A, B and C. The location and extent of the built environment is shown as shaded pale blue areas. In white solid lines we show the oldest fissures (4000BP-1599 CE) not used in these maps.



Training period	Testing period	Kernel function	smoothing h (m)	p -value
4000BP-1600CE	1601CE-present	Exp	1250	0.16
4000BP-1900CE	1901CE-present	Exp	1000	0.4
4000BP-1970CE	1971CE-present	Exp	500	0.14
1600CE-1900CE	1901CE-present	Exp	1000	0.23

Table 1. Different partitions of training and testing data explored (first two columns respectively). In the columns 3 and 4 we provide, for each partition, the pair of Kernel function and smoothing parameter value that well fit the ECDF of the distance to the nearest system of fissures in the training data, and is capable of explaining the testing data (p -values $>5\%$). See text.



Data set	Deformation model	Prob S Rift	Prob W Rift	Prob NE Rift	Prctile Point A	Prctile Point B	Prctile Point C
4000BP-present (Canonical model)	None	0.170 (0.0014)	0.075 (0.0018)	0.085 (0.0048)	99.3	99.3	97.0
4000BP-present	Vol	0.136 (0.0011)	0.088 (0.0021)	0.033 (0.0019)	99.3	99.3	97.4
4000BP-present	Flank	0.214 (0.0018)	0.012 (0.0003)	0.094 (0.0053)	98.2	98.5	98.4
4000BP-present	Both	0.164 (0.0014)	0.061 (0.0014)	0.053 (0.0031)	99.3	99.3	97.8
1600CE-present	None	0.112 (0.0009)	0.057 (0.0014)	0.114 (0.0065)	99.3	99.3	96.3
1600CE-present	Vol	0.116 (0.0010)	0.066 (0.0015)	0.033 (0.0019)	99.3	99.3	97.3
1600CE-present	Flank	0.160 (0.0013)	0.013 (0.0003)	0.144 (0.0081)	99.4	99.4	97.2
1600CE-present	Both	0.127 (0.0010)	0.051 (0.0012)	0.062 (0.0035)	99.3	99.3	97.4

Table 2. Columns 3-5: probability of future flank eruption in the different rifts (South, West and NorthEast respectively in columns 3, 4 and 5) and in parenthesis the probabilities normalized per km². Columns 6-8: Percentiles of the points A, B and C (respectively columns 6, 7 and 8) located at the three vents active in June 2022 on Etna (e.g., figure 8). The rift probabilities and the June 2022 vents' percentiles are relative to the spatial probability distribution for flank eruptions computed on different data periods (first column) and deformations source (second column).



Appendix

In this appendix we provide 6 figures related to some of the sensitivity analyses not shown in the main text. In Figure A1 we show the results of the analysis of the degree of clustering using other partitions of the data into training and testing dataset (different from those shown in the main text).

555 In Figure A2 we show the Reference models and the results of the sensitivity analysis to different sources of deformation for other partitions of the data into training and testing dataset (different from those shown in the main text).

In Figure A3 we show the canonical model in linear scale.

In Figure A4 we show the probability model achieved with the sensitivity test using only the last 400 years of data, in linear scale.

560 In Figure A5 we show the probability models, in linear scale, achieved with sensitivity tests on the canonical model based on different weighting of past fissures according to different sources of deformation.

In Figure A6 we show the probability models, in linear scale, achieved with sensitivity tests on the model based on different weighting of past fissures according to different sources of deformation and built on the last 400 years only.

We also provide a table (Table A1) with the polygons defining the three rifts, taken from Azzaro et al. (2012).

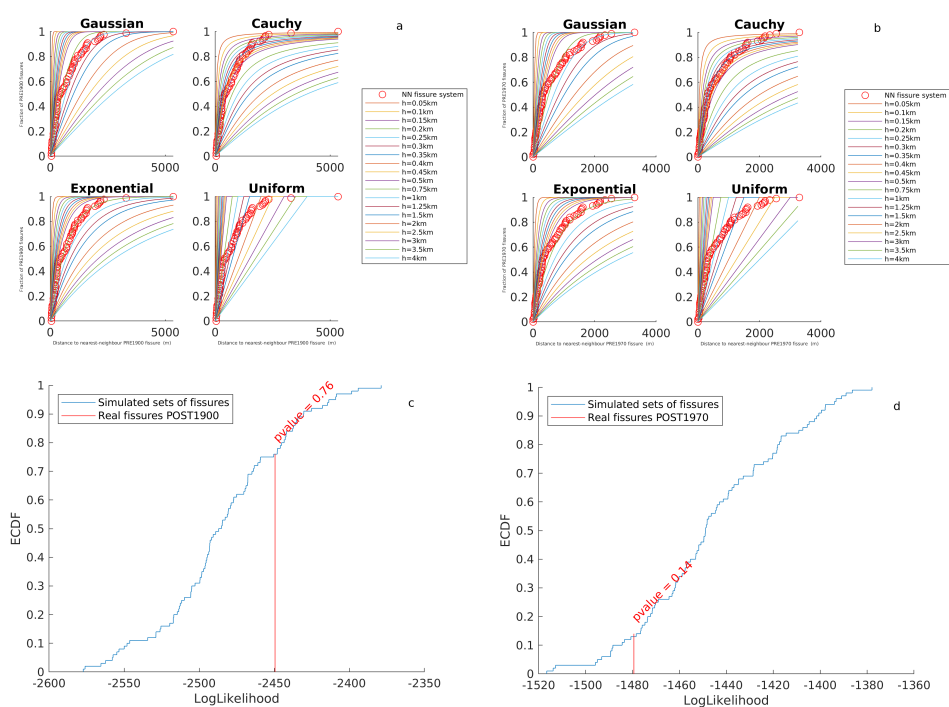


Figure A1. Panels a-b: Empirical Cumulative Density Functions (ECDF) of the distance to the nearest system of fissures (red dots) for the training period 4000BP-1900CE (a) and 4000BP-1970CE (b). The curves represent the theoretical cumulative for different kernel functions (Gaussian, Cauchy, Exponential and Uniform) and smoothing parameter h , as in legends on the right for each case. Panels c-d: ECDF of the Log-Likelihood of synthetic catalogs of synthetic fissures (black line) under the reference model for the training period (c) 4000BP-1900CE (Exponential kernel, $h=1000$ m) and (d) 4000BP-1970CE (Exponential kernel, $h=500$ m). In red we point the value of the Log-Likelihood achieved by the reference model on the real testing data, providing the p -value in percent.

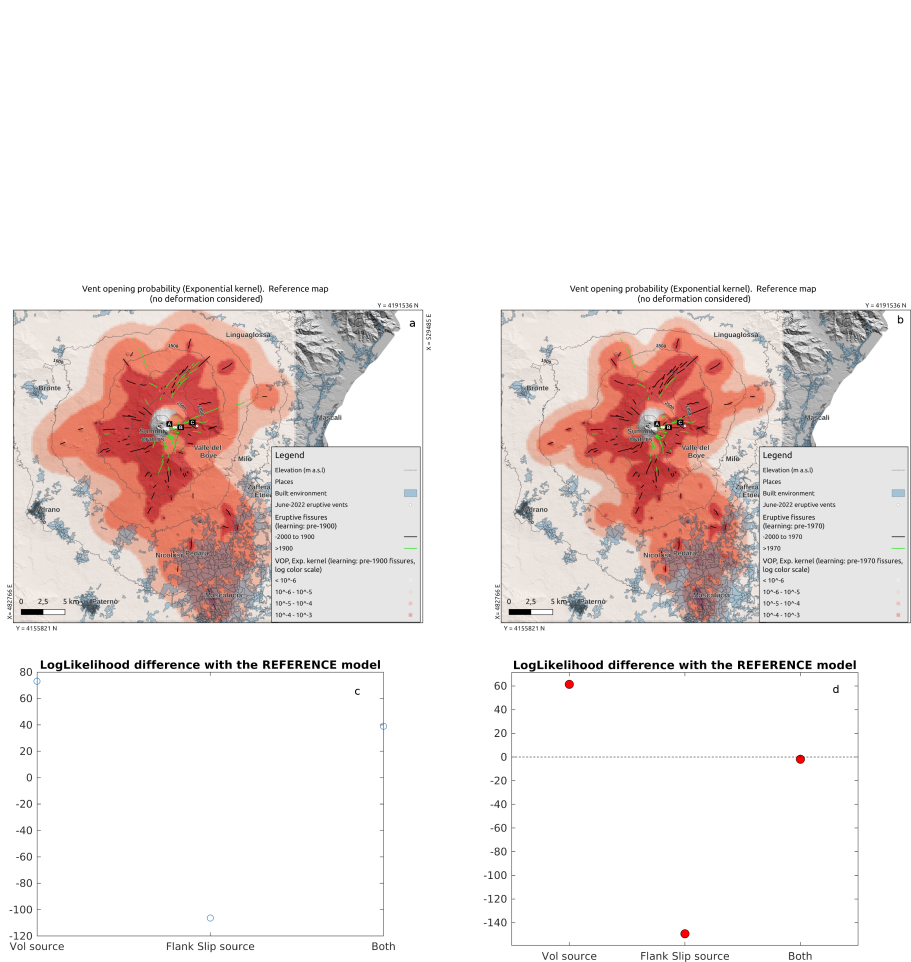


Figure A2. Panels a-b: Spatial probability (in Log-scale) distribution of flank opening under the reference model for the training period 4000BP-1900CE (a) and 4000BP-1970CE (b). In black and green the training and testing (i.e., respectively post 1900CE and post 1970CE for a and b) fissures. Panels c-d: Log-Likelihood difference between the models weighted with the three deformation sources explored (Volumetric, Flank Slip and Both) and the reference model of panels a and b, respectively. Positive differences (values above the dashed line) indicate a best performance on the testing data with respect of the reference model.

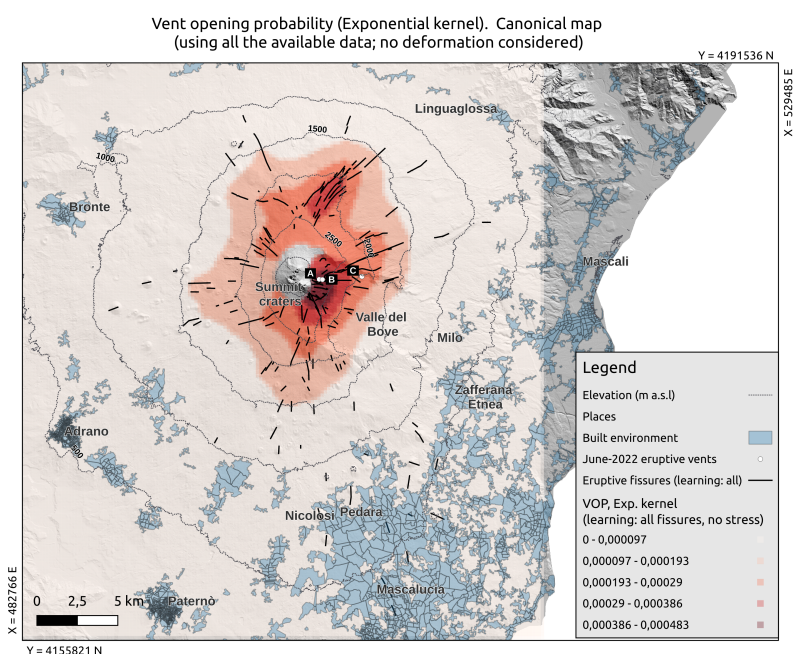


Figure A3. Same as Figure 7 but in linear scale: map of the probability (in linear scale) of flank fissure opening at Etna, based on the data 4000BP-present (black solid lines), in what we call canonical model. The location of the vents active in June 2022 is indicated by white points and labelled as A, B and C. The location and extent of the built environment is shown as shaded pale blue areas, and altitude contour lines are shown in dashed black lines.

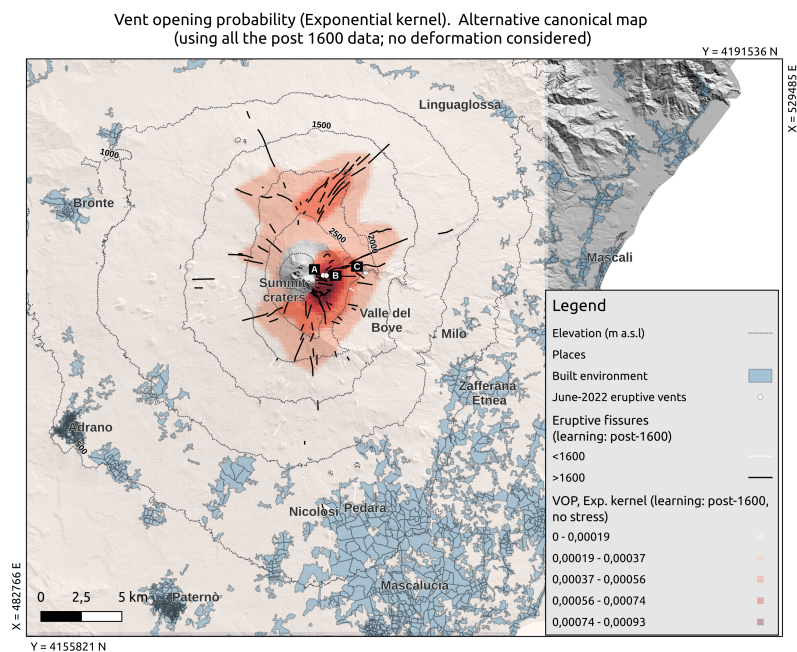


Figure A4. Same as Figure 8 but in linear scale: map of the probability (in linear scale) of flank fissure opening at Etna, based on a shorter time window for input data (1600CE-present, black solid lines). The location of the vents active in June 2022 is indicated by white points and labelled as A, B and C. The location and extent of the built environment is shown as shaded pale blue areas, and altitude contour lines are shown in dashed black lines.

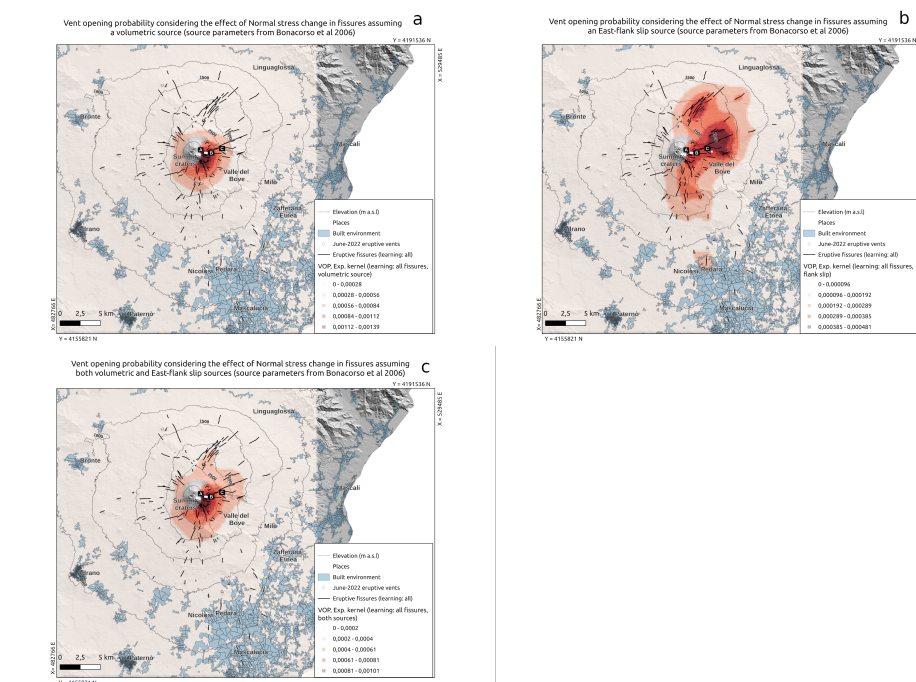


Figure A5. Same as Figure 9 but in linear scale: maps of the probability (in linear scale) of lateral fissure opening at Etna, based on the data 4000BP-present (black solid lines), considering the unclamping stress in the input fissures. The different panels a, b and c correspond to, respectively, information from the volumetric, flank-slip and both sources. In each panel, the location of the vents active in June 2022 is indicated by white points and labelled as A, B and C. The location and extent of the built environment is shown as shaded pale blue areas. In white solid lines we show the oldest fissures (4000BP-1599 CE) not used in these maps.

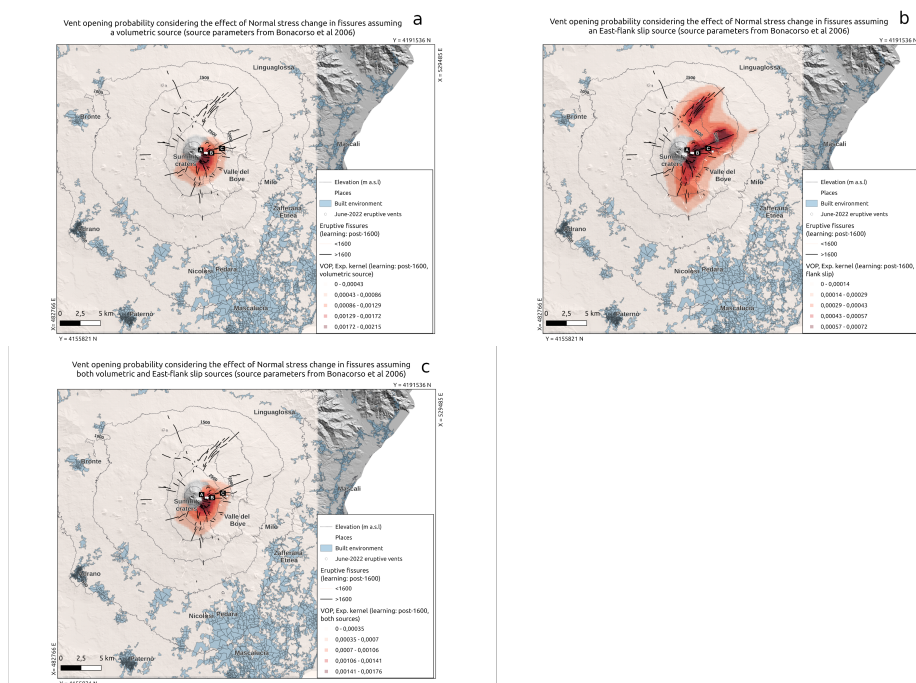


Figure A6. Same as Figure 10 but in linear scale: maps of the probability (in linear scale) of lateral fissure opening at Etna, based on the data 1600BP-present (black solid lines), considering the unclamping stress in the input fissures. The different panels a, b and c correspond to, respectively, information from the volumetric, flank-slip and both sources. In each panel, the location of the vents active in June 2022 is indicated by white points and labelled as A, B and C. The location and extent of the built environment is shown as shaded pale blue areas. In white solid lines we show the oldest fissures (4000BP-1599 CE) not used in these maps.



Rift name	Lon UTM (Easting)	Lat UTM (Northing)
South (S)	498995	4174932
	505687	4174168
	510198	4163548
	492739	4166057
West (W)	497576	4178606
	498086	4175660
	489247	4173259
	487938	4179333
North-East (NE)	500050	4182461
	4502923	4188172
	505869	4186644
	502014	4181516

Table A1. Points defining the polygons of the three rifts from Azzaro et al. (2012). Coordinates are given in UTM coordinates, 33T zone.